Performance Analysis of Slotless Axial Flux Permanent Magnet Machines with Skewed Magnets under Loading Condition

Farhad Rezaee-Alam*

Departement of Electrical Engineering, Lorestan University, 68151-44316, Khorramabad, Lorestan, Iran, +989166591727, Rezaee.fa@lu.ac.ir, farhad.rezaee.alam@gmail.com

Abstract

This paper presents a new 3D analytical technique for electromagnetic modeling and analysis the slotless axial flux permanent magnet (AFPM) machines. In the proposed technique, Laplace/Poisson equation is solved in different regions while considering the magnetic scalar potential as the main variable. To consider the curvature effect and radial dependency of permanent magnets (PMs), the 3D distribution of PM magnetization is introduced based on Fourier-Bessel series. The boundary conditions are then used to determine the unknown constants of Fourier-Bessel series in air-gap region. The influence of skewed PMs on the flux-linkage of stator phases is studied by using the proposed model under no-load condition while constant keeping the volume of PMs. The proposed 3D model is also extended to calculate the air-gap magnetic field due to stator currents and to extract the inductance matrix. The dynamic performance of studied slotless AFPM motor is then analyzed under voltage-input condition. In final, the accuracy of proposed 3D technique is verified by comparing the corresponding results obtained through proposed analytical model and 3D finite element method (FEM).

Index Terms: axial flux permanent magnet (AFPM) machine; flux-linkage; Fourier-Bessel series; magnetic field; magnetization; skew; slotless.

1. Introduction

3D analytical modeling is necessary for accurate electromagnetic analysis of axial flux permanent magnet (AFPM) machines due to their 3D structure [1]. 3D FEM is the famous technique for accurate modeling the AFPM machines, however it is time consuming [1]-[4]. In the case of optimization problem, which the 3D model should be repeatedly modified, 3D FEM is inefficient [4]-[5]. Due to complexity of 3D modeling and its time-consuming nature, multi-slice 2D FEM has been used to model and analysis of AFPM machines [6]-[8]. The multi-slice 2D analytical models including magnetic equivalent circuit (MEC) model [9]-[12], sub-domain (S-D) model [13], or conformal mappings (CMs) [14]-[15] have been also used for electromagnetic analysis the

AFPM machines. The main idea of multi-slice 2D FEM is based on varying the main dimension of AFPM machines along the radial direction. In multi-slice 2D technique, the 3D geometry of AFPM machines is approximated with 2D linear or rotating models at different radii. However, the effect of radial component of air-gap magnetic field, and the edge effect of overhang structure due to rotor PMs and coil end-turn cannot be accurately considered by using the multi-slice 2D technique.

To consider three components of air-gap magnetic field simultaneously, 3D MEC model was used to investigate the edge effect and non-linearity effect of iron parts in coreless AFPM motors [16]. However, the magnetic field can be only calculated at sparse points by using this 3D MEC model. The 3D S-D model has been also used in [17]-[18] for modeling the coreless AFPM machines with sector shaped PMs and slotless AFPM machines with halbach PMs, respectively. The S-D model acts based on dividing the geometry of AFPM machines into several domains, and solving the Laplace/Poisson equation in relevant domain. However, the radial edge effect has been neglected in previous references due to considering infinite value for radii of stator and rotor. This paper presents a new 3D S-D model based on finding the scalar magnetic potential due to PM poles and stator phases. The proposed technique acts based on dividing the AFPM geometry into several region in axial direction with different analytical length in radial direction. The stator coils are replaced with equivalent virtual PMs. The Fourier-Bessel series is then used to model the distribution of magnetization of skewed PM poles and equivalent virtual PMs (stator phases).

This paper is organized as follows:

The main parameters of analyzed slotless AFPM machine are introduced in section 2. The principles of 3D analytical model are presented in section 3. The performance analysis including the calculation of PM flux-linkage, stator inductances, stator phase currents, and electromagnetic torque by using proposed analytical model is presented in sections 4-5. The conclusions of work are given in section 6.

2. Parameters of Studied AFPM machine

The main parameters of analyzed single-sided 3-phases slotless AFPM machine with axial magnetized PMs are introduced in Table 1. A 3D view of studied AFPM machine with sector shaped PMs and radial coils, has been illustrated in Figure 1.

Figure 1

Table 1

3. Proposed 3D Analytical Model

For current free regions shown in Figure 2, Laplace equation in terms of scalar magnetic potential ψ in i^{th} region can be written as follows:

$$\nabla^2 \psi_i (r,\theta,z) = 0 \tag{1}$$

The necessary boundary condition in Figure 2 for solving (1) in the air-gap domain due to only PMs can be defined as shown in (2)-(4).

Figure 2

$$z = z_1 \rightarrow H_{t,3} = 0 \tag{2}$$

$$z = z_4 \rightarrow \begin{cases} H_{t,3} = H_{t,4} \\ B_{z,3} = B_{z,4} \end{cases} \tag{3}$$

$$z = z_5 \rightarrow H_{t,4} = 0 \tag{4}$$

Laplace equation (1) is solved by using the variable separation method while assuming the stator and rotor cores in slotless AFPM machine have the infinite magnetic permeability. To consider the edge effect, the regions in Figure 2 have different radius from others. The general solution of (1) in terms of Fourier-Bessel series in i^{th} region can be written as follows:

$$\psi_i (r,\theta,z) = \sum_k \sum_l \left[\begin{array}{l} \left(L_i (k,l) e^{\frac{j_{(k,l)}}{r_a} z} + M_i (k,l) e^{-\frac{j_{(k,l)}}{r_a} z} \right) J_l \left(\frac{j_{(k,l)}}{r_a} r \right) cos(l\theta) \\ + \left(N_i (k,l) e^{\frac{j_{(k,l)}}{r_a} z} + O_i (k,l) e^{-\frac{j_{(k,l)}}{r_a} z} \right) J_l \left(\frac{j_{(k,l)}}{r_a} r \right) sin(l\theta) \end{array} \right] \tag{5}$$

where, r, θ and z are the coordinates of a typical point, r_a is the radial length of air-gap, $j_{(k,l)}$ is the k[th] root of first-kind Bessel function $J_l (r)$. The unknown constants $L_{i,(k,l)}, M_{i,(k,l)}$, $N_{i,(k,l)}$, and $O_{i,(k,l)}$ are respectively the value of element in k[th] row and $(l+1)^{th}$ column of the

matrix L_i , M_i , N_i and O_i , all in i^{th} region. The magnetic field strength in i^{th} region can be calculated by using following formula:

$$\vec{H} = -\vec{\nabla}\psi = -\frac{\partial \psi}{\partial r}\vec{a}_r - \frac{1}{r}\frac{\partial \psi}{\partial \theta}\vec{a}_\theta - \frac{\partial \psi}{\partial z}\vec{a}_z \tag{6}$$

$$H_{r,i}(r,\theta,z) = -\sum_k \sum_l \left(\frac{j_{(k,l)}}{2r_a}\right) \left[\begin{array}{l} \left(L_i(k,l) e^{\frac{j_{(k,l)}}{r_a} z} + M_i(k,l) e^{-\frac{j_{(k,l)}}{r_a} z} \right) F\left(\frac{j_{(k,l)}}{r_a} r\right) \cos(l\theta) \\ + \left(N_i(k,l) e^{\frac{j_{(k,l)}}{r_a} z} + O_i(k,l) e^{-\frac{j_{(k,l)}}{r_a} z} \right) F\left(\frac{j_{(k,l)}}{r_a} r\right) \sin(l\theta) \end{array} \right] \tag{7}$$

$$H_{t,i}(r,\theta,z) = \sum_k \sum_l \left(\frac{l}{r}\right) \left[\begin{array}{l} \left(L_i(k,l) e^{\frac{j_{(k,l)}}{r_a} z} + M_i(k,l) e^{-\frac{j_{(k,l)}}{r_a} z} \right) J_l\left(\frac{j_{(k,l)}}{r_a} r\right) \sin(l\theta) \\ - \left(N_i(k,l) e^{\frac{j_{(k,l)}}{r_a} z} + O_i(k,l) e^{-\frac{j_{(k,l)}}{r_a} z} \right) J_l\left(\frac{j_{(k,l)}}{r_a} r\right) \cos(l\theta) \end{array} \right] \tag{8}$$

$$H_{z,i}(r,\theta,z) = -\sum_k \sum_l \left(\frac{j_{(k,l)}}{r_a}\right) \left[\begin{array}{l} \left(L_i(k,l) e^{\frac{j_{(k,l)}}{r_a} z} - M_i(k,l) e^{-\frac{j_{(k,l)}}{r_a} z} \right) J_l\left(\frac{j_{(k,l)}}{r_a} r\right) \cos(l\theta) \\ + \left(N_i(k,l) e^{\frac{j_{(k,l)}}{r_a} z} - O_i(k,l) e^{-\frac{j_{(k,l)}}{r_a} z} \right) J_l\left(\frac{j_{(k,l)}}{r_a} r\right) \sin(l\theta) \end{array} \right] \tag{9}$$

The components of $\vec{H}$ is obtained as shown in (7)-(9). $F\left(\frac{j_{(k,l)}}{r_a} r\right)$ in (7) is defined as shown in (10).

$$F\left(\frac{j_{(k,l)}}{r_a} r\right) = J_{l-1}\left(\frac{j_{(k,l)}}{r_a} r\right) - J_{l+1}\left(\frac{j_{(k,l)}}{r_a} r\right) \tag{10}$$

As shown in Figure 2, the PM magnetization $\left(\vec{M}\right)$ should be considered in region 4 to calculate the magnetic flux density as follows:

$$\begin{cases} \overrightarrow{B} = \mu_{\circ}\left(\overrightarrow{H} + \overrightarrow{M}\right) \\ \overrightarrow{M} = M_z \overrightarrow{a_z} \end{cases} \tag{11}$$

In (11), $\mu_{\circ}$ is the magnetic permeability of air. The Fourier-Bessel series is used to express the distribution of axial magnetization of PMs, as shown in (12).

$$\begin{aligned} M_z &= -0.5\sum_k a_{(k,0)} J_0\left(\frac{j_{(k,0)}}{r_a} r\right) \\ &+ \sum_k \sum_l \left[a_{(k,l)} J_l\left(\frac{j_{(k,l)}}{r_a} r\right) cos\left(l\theta\right) + b_{(k,l)} J_l\left(\frac{j_{(k,l)}}{r_a} r\right) sin\left(l\theta\right) \right] \\ a_{(k,l)} &= \frac{2}{\pi {r_a}^2 \left[J_{l+1}\left(j_{(k,l)}\right)\right]^2} \int_0^{2\pi} \int_0^{r_a} r M_z J_l\left(\frac{j_{(k,l)}}{r_a} r\right) cos\left(l\theta\right) dr d\theta \\ b_{(k,l)} &= \frac{2}{\pi {r_a}^2 \left[J_{l+1}\left(j_{(k,l)}\right)\right]^2} \int_0^{2\pi} \int_0^{r_a} r M_z J_l\left(\frac{j_{(k,l)}}{r_a} r\right) sin\left(l\theta\right) dr d\theta \end{aligned} \tag{12}$$

$$\begin{cases} e^{\left(\frac{j_{(k,l)}}{r_a} z_4\right)} \times L_{4,(k,l)} + e^{\left(-\frac{j_{(k,l)}}{r_a} z_4\right)} \times M_{4,(k,l)} = 0 \\ e^{\left(\frac{j_{(k,l)}}{r_a} z_4\right)} \times N_{4,(k,l)} + e^{\left(-\frac{j_{(k,l)}}{r_a} z_4\right)} \times O_{4,(k,l)} = 0 \\ e^{\left(\frac{j_{(k,l)}}{r_a} z_3\right)} \times L_{3,(k,l)} - e^{\left(\frac{j_{(k,l)}}{r_a} z_3\right)} \times L_{4,(k,l)} + e^{\left(-\frac{j_{(k,l)}}{r_a} z_3\right)} \times M_{3,(k,l)} - e^{\left(-\frac{j_{(k,l)}}{r_a} z_3\right)} \times M_{4,(k,l)} = 0 \\ e^{\left(\frac{j_{(k,l)}}{r_a} z_3\right)} \times N_{3,(k,l)} - e^{\left(\frac{j_{(k,l)}}{r_a} z_3\right)} \times N_{4,(k,l)} + e^{\left(-\frac{j_{(k,l)}}{r_a} z_3\right)} \times O_{3,(k,l)} - e^{\left(-\frac{j_{(k,l)}}{r_a} z_3\right)} \times O_{4,(k,l)} = 0 \\ -e^{\left(\frac{j_{(k,l)}}{r_a} z_3\right)} \times L_{3,(k,l)} + e^{\left(\frac{j_{(k,l)}}{r_a} z_3\right)} \times L_{4,(k,l)} + e^{\left(-\frac{j_{(k,l)}}{r_a} z_3\right)} \times M_{3,(k,l)} - e^{\left(-\frac{j_{(k,l)}}{r_a} z_3\right)} \times M_{4,(k,l)} = \left(\frac{r_a}{j_{(k,l)}}\right) \times a_{(k,l)} \\ -e^{\left(\frac{j_{(k,l)}}{r_a} z_3\right)} \times N_{3,(k,l)} + e^{\left(\frac{j_{(k,l)}}{r_a} z_3\right)} \times N_{4,(k,l)} + e^{\left(-\frac{j_{(k,l)}}{r_a} z_3\right)} \times O_{3,(k,l)} - e^{\left(-\frac{j_{(k,l)}}{r_a} z_3\right)} \times O_{4,(k,l)} = \left(\frac{r_a}{j_{(k,l)}}\right) \times b_{(k,l)} \\ e^{\left(\frac{j_{(k,l)}}{r_a} z_1\right)} \times L_{3,(k,l)} + e^{\left(-\frac{j_{(k,l)}}{r_a} z_1\right)} \times M_{3,(k,l)} = 0 \\ e^{\left(\frac{j_{(k,l)}}{r_a} z_1\right)} \times N_{3,(k,l)} + e^{\left(-\frac{j_{(k,l)}}{r_a} z_1\right)} \times O_{3,(k,l)} = 0 \end{cases} \tag{13}$$

Figure 3

Figure 4

For a non-skewed trapezoid PM pole of analyzed AFPM machine, the real distribution of M_z and the approximated distribution based on Fourier-Bessel series are shown in Figure 3. To calculate the distribution of air-gap magnetic field due to only PM poles, the unknown constants in (7)-(9) should be determined through applying the boundary condition. The unknown constants for regions of air-gap and PMs are determined from solving (13). For a typical operating point, the components of air-gap flux density due to only rotor PMs are shown in Figure 4.

To calculate the air-gap magnetic field due to stator phases by using the proposed analytical model, the stator coils are replaced with virtual equivalent PMs while maintaing the magneto motive force (MMF) of stator coils. The remanence of virtual equivalent PMs can be calculated as follows:

$$N_t \times I_c = \frac{B_R}{\mu_\circ} \times h_c \rightarrow B_R = \frac{\mu_\circ \times N_t \times I_c}{h_c} \tag{14}$$

where N_t, I_c and h_c are respectively the number of turns, the magnitude of coil current, and the height of relevant coil. For example, for one stator coil which is carrying one ampere current $\left(I_c = 1(A)\right)$, the 3D distribution of turn function and the 3D distribution of magnetization of equivalent virtual PM are shown in Figure 5. To calculate the armature reaction magnetic field, the boundary conditions (15)-(17) should be applied in Figure 2, to determine the unknown constants in (7)-(9) through solving the system of equations (18).

Figure 5

For a typical operating point under loading condition when the root mean square (RMS) value of phase currents is 4(A) and the power factor is equal to 0.46 lag ($I_A = 0.586\,(A), I_B = -6.497\,(A), I_C = 1.575\,(A)$), the componets of air-gap magnetic field due to only the armature reaction are shown in Figure 6.

$$z = z_1 \rightarrow H_{t,2} = 0 \tag{15}$$

$$z = z_2 \rightarrow \begin{cases} H_{t,2} = H_{t,3} \\ B_{z,2} = B_{z,3} \end{cases} \tag{16}$$

$$z = z_4 \rightarrow H_{t,3} = 0 \tag{17}$$

The edge effect due to the radial component of armature reaction field is illustrated in Figure 6c (r=100 mm). In real, B_r of armature reaction field is negligible for the analyzed slotless AFPM motor in the middile of air-gap (r=125 mm). For every operating point, the total air-gap magnetic field is equal to the sum of air-gap field due to rotor PMs and stator phases.

Figure 6

$$
\begin{cases}
e^{\left(\frac{j_{(k,l)}}{r_a}z_1\right)}\times L_{2,(k,l)}+e^{\left(-\frac{j_{(k,l)}}{r_a}z_1\right)}\times M_{2,(k,l)}=0 \\
e^{\left(\frac{j_{(k,l)}}{r_a}z_1\right)}\times N_{2,(k,l)}+e^{\left(-\frac{j_{(k,l)}}{r_a}z_1\right)}\times O_{2,(k,l)}=0 \\
e^{\left(\frac{j_{(k,l)}}{r_a}z_2\right)}\times L_{2,(k,l)}-e^{\left(\frac{j_{(k,l)}}{r_a}z_2\right)}\times L_{3,(k,l)}+e^{\left(-\frac{j_{(k,l)}}{r_a}z_2\right)}\times M_{2,(k,l)}-e^{\left(-\frac{j_{(k,l)}}{r_a}z_2\right)}\times M_{3,(k,l)}=0 \\
e^{\left(\frac{j_{(k,l)}}{r_a}z_2\right)}\times N_{2,(k,l)}-e^{\left(\frac{j_{(k,l)}}{r_a}z_2\right)}\times N_{3,(k,l)}+e^{\left(-\frac{j_{(k,l)}}{r_a}z_2\right)}\times O_{2,(k,l)}-e^{\left(-\frac{j_{(k,l)}}{r_a}z_2\right)}\times O_{3,(k,l)}=0 \\
e^{\left(\frac{j_{(k,l)}}{r_a}z_2\right)}\times L_{2,(k,l)}-e^{\left(\frac{j_{(k,l)}}{r_a}z_2\right)}\times L_{3,(k,l)}-e^{\left(-\frac{j_{(k,l)}}{r_a}z_2\right)}\times M_{2,(k,l)}+e^{\left(-\frac{j_{(k,l)}}{r_a}z_2\right)}\times M_{3,(k,l)}=\left(\frac{r_a}{j_{(k,l)}}\right)\times a_{(k,l)} \\
e^{\left(\frac{j_{(k,l)}}{r_a}z_2\right)}\times N_{2,(k,l)}-e^{\left(\frac{j_{(k,l)}}{r_a}z_2\right)}\times N_{3,(k,l)}-e^{\left(-\frac{j_{(k,l)}}{r_a}z_2\right)}\times O_{2,(k,l)}+e^{\left(-\frac{j_{(k,l)}}{r_a}z_2\right)}\times O_{3,(k,l)}=\left(\frac{r_a}{j_{(k,l)}}\right)\times b_{(k,l)} \\
e^{\left(\frac{j_{(k,l)}}{r_a}z_4\right)}\times L_{3,(k,l)}+e^{\left(-\frac{j_{(k,l)}}{r_a}z_4\right)}\times M_{3,(k,l)}=0 \\
e^{\left(\frac{j_{(k,l)}}{r_a}z_4\right)}\times N_{3,(k,l)}+e^{\left(-\frac{j_{(k,l)}}{r_a}z_4\right)}\times O_{3,(k,l)}=0
\end{cases}
\tag{18}
$$

4. Proposed 3D Analytical Model

For no-load analysis, the PM flux-linkage with stator phases can be calculated using (19) while considering different skew angles of trapezoid PM poles.

$$\lambda_m(\theta_r)=\int_0^{2\pi}\int_{r_{si}}^{r_{so}} N_i(r,\theta)\times B_z(r,\theta)\times ds(r,\theta) \tag{19}$$

where $N_i(r,\theta)$ is the distribution of turn function of i^{th} phase winding, $B_z(r,\theta)$ is the axial component of air-gap flux density due to PM poles, and $ds(r,\theta)$ is the area of differential element at the coordinate of (r,θ).

To study the effect of skewed trapezoid PMs on the flux-linkage of stator phases, different skew angles from 5° to 30° are applied to the rotor PMs while having a constant value for volume of PMs. Figure 7 shows an illustration of one skewed PM. As shown, the volume of PM has not been varied due to the skewing effect.

Figure 7

To calculate the components of air-gap magnetic field due to skewed trapezoid PMs, the distribution of PM magnetization should be firstly expressed into Fourier-Bessel series. For example, for one skewed trapezoid PM with $\theta_{sk} = 20^\circ$, the real and approximated distribution of PM magnetization are shown in Figure 8. All steps of magnetic field calculation by using the proposed analytical technique have been explained in section 3. The results of PM flux-linkage with one stator phase obtained through (19) have been shown and compared in Figure 9 and Table 2 while considering different skew angles for PM poles.

Figure 8

Figure 9

Table 2

The accurate comparison of PM flux linkage results based on Fourier analysis and total harmonic distortion (THD) has been presented in Table 2 without any change in the volume of PM poles.

As shown in Table 2, the wave form of λ_m becomes more sinusoidal when increasing the skew angle. However, the amplitude of main harmonic of λ_m is reduced somewhat due to skewing effect. It should be noted that the allowable maximum value of θ_{sk} is 30°due to limitation of PM geometry.

5. On-load Analysis with Skewed PMs

For on-load analysis, one three-phase voltage source with RMS value of 35 (V) is applied to the stator phases while rotating the rotor at the synchronous speed, which is equal to 375 (rpm). Under

this condition, the system of electrical equations for analyzed slotless AFPM motor can be written as follows:

$$\begin{cases} V = R \times I + \dfrac{d\Lambda}{dt} \\ \Lambda = L \times I + \Lambda_m \end{cases} \rightarrow V = R \times I + L \times \frac{dI}{dt} + \frac{d\Lambda_m}{dt} \tag{20}$$

where $V = [V_S]_{3*1}$ is the matrix of three-phase voltage sources, $I = [I_S]_{3*1}$ is the matrix of three-phase currents, $\Lambda = [\lambda_S]_{3*1}$ is the matrix of three-phase flux-linkage, $\Lambda_m = [\lambda_m]_{3*1}$ is the matrix of three-phase PM flux-linkage, $L = [L_S]_{3*3}$ is the inductance matrix of stator, and $R = [R_S]_{3*3}$ is the resistance matrix of three-phase winding.

The finite difference method (FDM) is then used to transform the differential equations (20) into recursive algebraic equations as follows [19]:

$$\begin{aligned} & V(t) = R \times I(t) + L \times \frac{I(t+\Delta t) - I(t)}{\Delta t} + \frac{\Lambda_m(t) - \Lambda_m(t-\Delta t)}{\Delta t} \rightarrow \\ & I(t+\Delta t) = I(t) + [L]^{-1} \times \left[\Delta t \times \left(V(t) - R \times I(t) \right) + \Lambda_m(t-\Delta t) - \Lambda_m(t) \right] \end{aligned} \tag{21}$$

where Δt is the time-step of simulation.

To extract the phase currents, it is firstly necessary to calculate the self and mutual inductances of stator phases as follows:

$$\begin{cases} L_{A-A} = \left. \dfrac{\lambda_A}{I_A} \right| I_A \neq 0, I_B = 0, I_C = 0, \ PMs \quad are \quad removed = 3.45(mH) \\ L_{A-B} = \left. \dfrac{\lambda_A}{I_B} \right| I_B \neq 0, I_A = 0, I_C = 0, \ PMs \quad are \quad removed = -0.46(mH) \end{cases} \tag{22}$$

In (22), λ_A is calculated through (19) while replacing the stator coils of phase A with equivalent virtual PMs. As shown, the elements of inductance matrix are constant values for slotless AFPM machines. For every operating point, the Maxwell Stress Tensor (MST) method [20] can be used to calculate the electromagnetic torque as follows:

$$T_e = \frac{1}{\mu_o} \int_{r_{ri}}^{r_{ro}} \int_{0}^{2\pi} B_t(r,\theta) \times B_z(r,\theta) \times r^2 dr d\theta \tag{23}$$

The analyzed slotless AFPM motor is supplied with one three-phase voltage source (V_{RMS}=35 (V)) at synchronous speed 375 (rpm), so that the RMS value of phase current in steady state is to be 4

(A). Under these conditions, the phase current and electromagnetic torque of analyzed AFPM motor are shown in Figure 10 while considering different skew angles of PM poles. A more detailed study of the effect of skew angle of PM poles on the dynamic performance of analyzed slotless AFPM motor has been presented in Table 3. As shown, the input power factor and the THD of phase current decrease whereas the electromagnetic torque remains nearly constant as the skew angle increases.

Figure 10

Table 3

To verify the accuracy of proposed 3D analytical model, the optimal results of analyzed soltless AFPM motor (with $\theta_{sk} = 30^{o}$) under no-load and on-load conditions have been compared with corresponding results obtained through 3D FEM, as shown in Figure 11.

Figure 11

6. Conclusion

This paper proposed a new 3D analytical model based on scalar magnetic potential for electromagnetic analysis of slotless AFPM machines under loading condition. The geometry of AFPM machine was divided into several regions, and Laplace's equation was solved in air-gap region to determine the air-gap flux density components due to rotor PMs and armature reaction. To consider different magnet shaping due to the skewing effect, the 3D distribution of PM magnetization was expressed into Fourier-Bessel series. For this reason, the general solution of Laplace's equation was also expressed into Fourier-Bessel series. The stator coils were replaced with equivalent virtual PMs to calculate the armature reaction field in air-gap and the inductance matrix. The magnetic field results obtained through proposed 3D model were then used to analyze the dynamic performance of analyzed slotless AFPM motor. The proposed approach can be also used to consider the other shapes of PM and coils for 3D electromagnetic analysis of slotless AFPM machines. The no-load results showed the more sinusoidal PM flux-linkage is obtained by using the skewed PMs with a miximum reduction in main component about 6 percent. It was also seen that the input power factor and the THD of stator phase current are decreased due to the skewing effect when the sinusoidal three-phase voltage source is applied to the stator windings.

7. References

[1]. Huang, R., Song, Z., Zhao, H., and et al., "Overview of axial flux machines and modeling methods," *IEEE Trans. Transport. Electrific.*, **8**(2), pp. 2118-2132 (2022). DOI: https://doi.org/10.1109/TTE.2022.3144594.

[2]. Aydin, M., Zhu, Z. Q., Lipo, T. A., and et al., "Minimization of Cogging Torque in Axial-Flux Permanent-Magnet Machines: Design Concepts", *IEEE Trans. Magn.*, **43**(9), pp. 3614-3622, (2007). DOI: https://doi.org/10.1109/TMAG.2007.902818.

[3]. Zakir, M. R., Ikram, J., Shah, S. I., and et al., "Performance Improvement of Axial Flux Permanent Magnet Machine with Phase Group Concentrated Coil Winding", *Energies*, **15**(19), (2022). DOI: https://doi.org/10.3390/en15197337.

[4]. Yu, F., Chen, H., Yan, W., and et al., "Design and Multiobjective Optimization of a Double-Stator Axial Flux SRM with Full-Pitch Winding Configuration", *IEEE Trans. Transport. Electrific.*, **8**(4), pp. 4348-4364, (2022). DOI: https://doi.org/10.1109/TTE.2022.3173938.

[5]. Mahmood, Z., Ikram, J., Badar, R., and et al., "Minimization of Torque Ripples in Multi-Stack Slotted Stator Axial-Flux Synchronous Machine by Modifying Magnet Shape", *Mathematics*, **10**(10), (2022). DOI: https://doi.org/10.3390/math10101653.

[6]. Gulec, M., and Aydin, M., "Implementation of different 2D finite element modelling approaches in axial flux permanent magnet disc machines", *IET Electr. Power Appl.*, **12**(2), pp. 195-202, (2018). DOI: https://doi.org/10.1049/iet-epa.2017.0434.

[7]. Kim, K. H., and Woo, D. K., "Novel Quasi-Three-Dimensional Modeling of Axial Flux In-Wheel Motor With Permanent Magnet Skew", *IEEE Access*, **10**, pp. 98842-98854, (2022). DOI: https://doi.org/10.1109/ACCESS.2022.3206774.

[8]. Hao, Z., Ma, Y., Wang, P., and et al., "A Review of Axial-Flux Permanent-Magnet Motors: Topological Structures, Design, Optimization and Control Techniques", *Machines*, **10**(12), (2022). DOI: https://doi.org/10.3390/machines10121178.

[9]. Kano, Y., Kosaka, T., and Matsui, N., "A Simple Nonlinear Magnetic Analysis for Axial-Flux Permanent-Magnet Machines", *IEEE Trans. Ind. Electron.*, **57**(6), pp. 2124-2133, (2010). DOI: https://doi.org/10.1109/TIE.2009.2034685.

[10]. Li, Q., Liu, A., and Zhang, B., "Analysis of a Combined-Type Axial-Flux Permanent Magnet Machine", *IEEE Access*, **10**, pp. 32022-32033, (2022). DOI: https://doi.org/10.1109/ACCESS.2022.3160478.

[11]. Tong, W., Wang, S., Dai, S., and et al., "A Quasi 3-D Magnetic Equivalent Circuit Model of a Double-Sided Axial Flux Permanent Magnet Machine Considering Local Saturation", *IEEE Trans. Energy Convers.*, **33**(4), pp. 2163-2173, (2018). DOI: https://doi.org/10.1109/TEC.2018.2853265.

[12]. Huang, R., Song, Z., Dong, Z., and et al. "An Improved Magnetic Equivalent Circuit Method for Segmented-Halbach Axial-Flux Permanent Magnet Machines", *IEEE Trans. Transport. Electrific.*, **9**(2), pp. 3218-3227, (2023). DOI: https://doi.org/10.1109/TTE.2022.3223960.

[13]. Guo, B., Du, Y., Djelloul-Khedda, Z., and et al., "Nonlinear Semianalytical Model for Axial Flux Permanent-Magnet Machine", *IEEE Trans. Ind. Electron.*, **69**(10), pp. 9804-9816, (2022). DOI: https://doi.org/10.1109/TIE.2022.3159952.

[14]. Guo, B., Huang, Y., Peng, F., and et al., "Analytical Modeling of Manufacturing Imperfections in Double Rotor Axial Flux PM Machines: Effects on Back EMF", *IEEE Trans. Magn.*, 53(6), (2017). DOI: https://doi.org/10.1109/TMAG.2017.2659762.

[15]. Shahbazi Ayat, Y., and Alizadeh Pahlavani, M. R., “3D computation of no-load magnetic flux density in slotless axial-flux permanentmagnet synchronous machines using conformal mapping”, *IET Electr. Power Appl.*, **11**(8), pp. 1391-1396, (2017). DOI: https://doi.org/10.1049/iet-epa.2016.0772.

[16]. Zhao, J., Ma, T., Liu, X., and et al., “Performance Analysis of a Coreless Axial-Flux PMSM by An Improved Magnetic Equivalent Circuit Model”, *IEEE Trans. Energy Convers.*, **36**(3), pp. 2120-2130, (2021). DOI: https://doi.org/10.1109/TEC.2020.3040009.

[17]. Huang, Y., Ge, B., Dong, J., and et al., "3-D Analytical Modeling of No-Load Magnetic Field of Ironless Axial Flux Permanent Magnet Machine", *IEEE Trans. Magn.*, **48**(11), pp. 2929-2932, (2012). DOI: https://doi.org/10.1109/TMAG.2012.2194699.

[18]. Jin, P., Yuan, Y., Xu, Q., and et al., "Analysis of Axial-Flux Halbach Permanent-Magnet Machine", *IEEE Trans. Magn.*, **51**(11), (2015). DOI: https://doi.org/10.1109/TMAG.2015.2449352.

[19]. Rezaee-Alam, F., Hamidi, A., and Hosseini, M., “A New Hybrid Analytical Model Based on Winding Function Theory for Analysis of Unbalanced Two-Phase Induction Motors”, *Scientia Iranica*, **31**(2), pp. 149-160, (2024). DOI: https://doi.org/10.24200/sci.2022.57654.5348.

[20]. Cheng, W., Cao, G., Deng, Z., and et al., “Torque Comparison Between Slotless and Slotted Ultra-high Speed AFPM Motors Using Analytical Method”, *IEEE Trans. Magn.*, **58**(2), (2022). DOI: https://doi.org/10.1109/TMAG.2021.3081175.

Figure 1. A shematic of slotless AFPM machine

Figure 2. 2D cross section of slotless AFPM machine, (a) R-φ plane, (b) R-Z plane

Figure 3. Distribution of M_z, (a) Real distribution, (b) Approximated distribution

Figure 4. Air-gap flux density components due to PMs (r=125 mm), (a) z-component, (b) t-component, (c) r-component

Figure 5. Equating a coil with one virtual PM, (a) Distribution of turn function, (b) Distribution of equivalent virtual PM

Figure 6. Armature reaction magnetic field, (a) axial component (r=125 mm), (b) tangential component (r=125 mm), (c) radial component (r=100 mm)

Figure 7. Illustration of un-skewed and skewed PM, (a) Un-skewed PM, (b) Skewed PM

Figure 8. Distribution of magnetization for one skewed PM ($\theta_{sk} = 20^{\circ}$), (a) Real distribution, (b) Approximated distribution

Figure 9. PM flux-linkage of stator phase

Figure 10. Results of dynamic performance, (a) stator phase current, (b) electromagnetic torque

Figure 11. Verification of proposed model, (a) PM flux-linkage with stator phase, (b) stator phase current, (c) electromagnetic torque

Table 1. Main parameters of analyzed AFPM machine

Table 2: Skew Effect on PM flux-linkage

Table 3: Skew Effect on Dynamic Performance

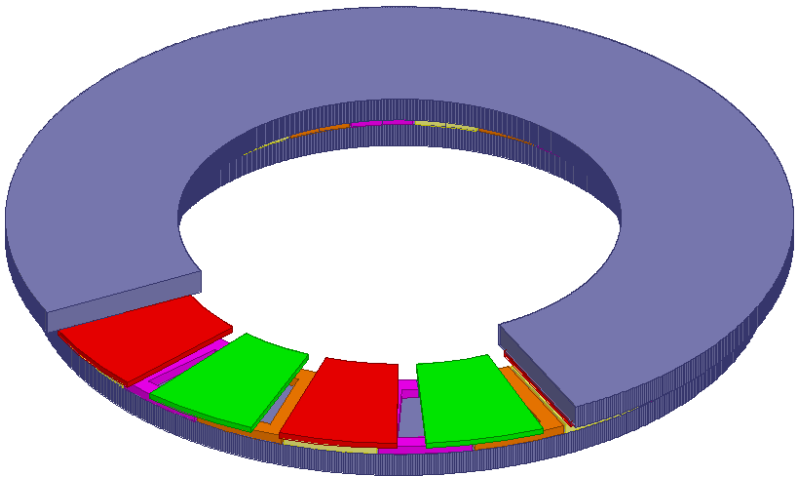

Figure 1

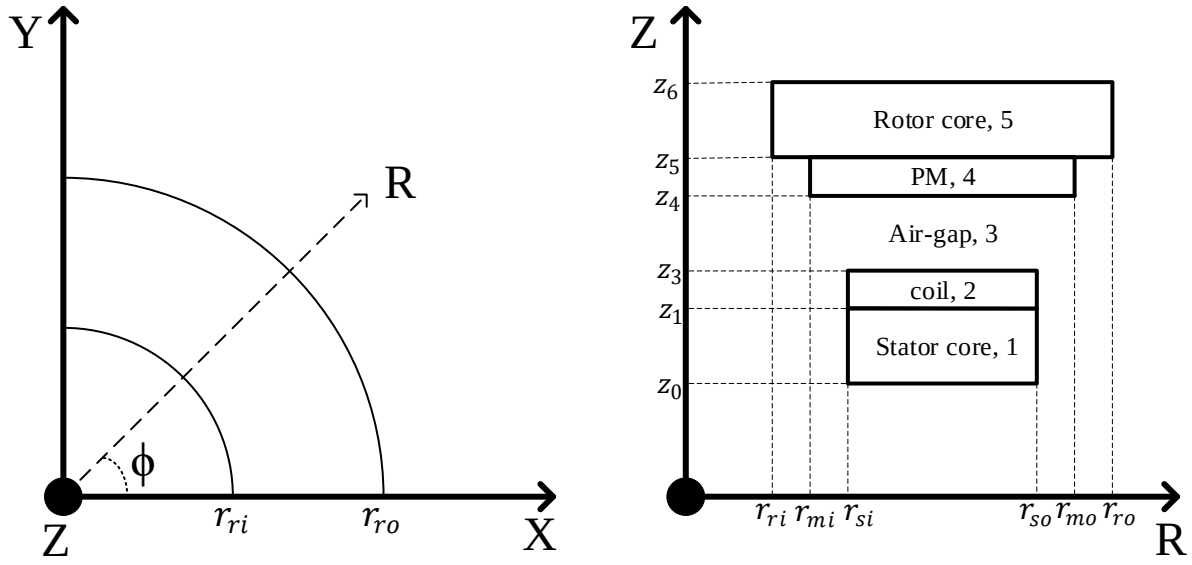
Y
R
ϕ
Z
r_{ri}
r_{ro}
X
Z
z_6
Rotor core, 5
z_5
PM, 4
z_4
Air-gap, 3
z_3
coil, 2
z_1
Stator core, 1
z_0
r_{ri} r_{mi} r_{si}
r_{so} r_{mo} r_{ro}
R

(a) (b)

Figure 2

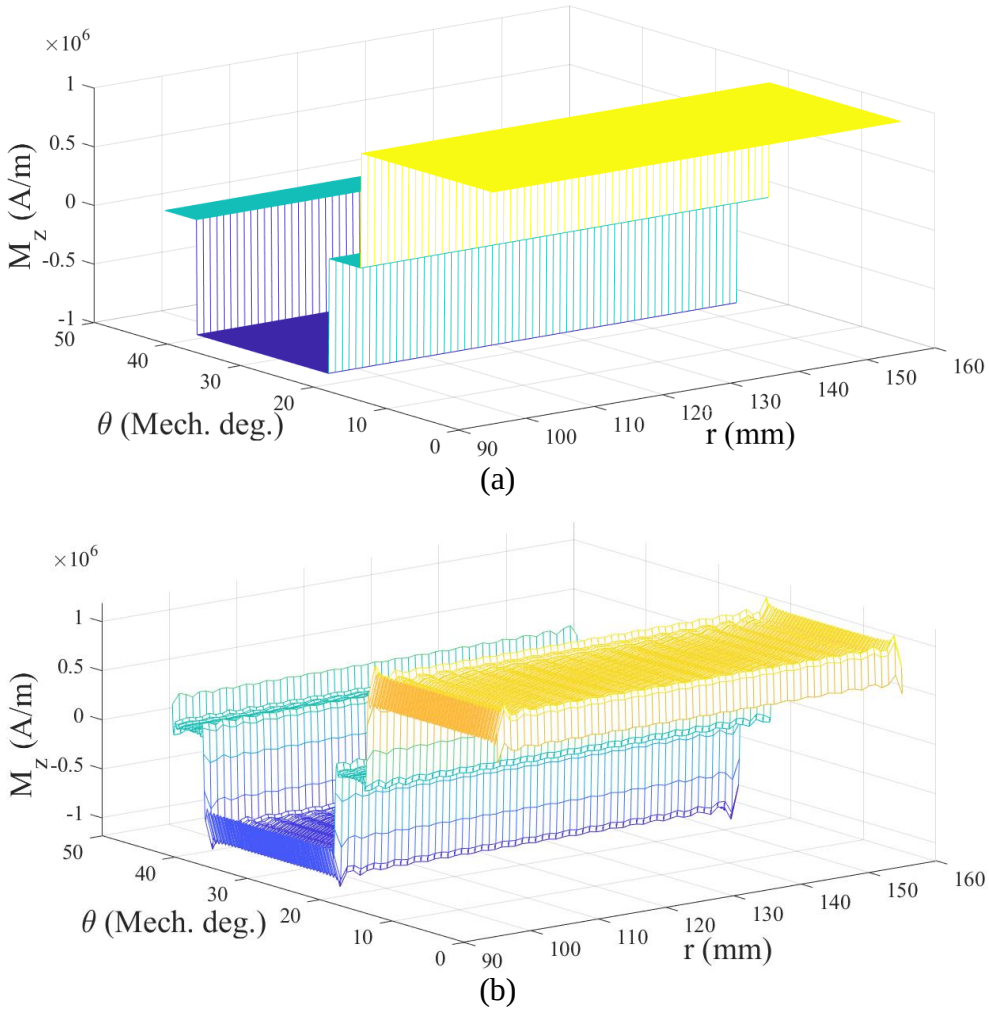
×10^6
1
0.5
0
-0.5
-1
M_z (A/m)
50
40
30
20
10
0
θ (Mech. deg.)
90
100
110
120
130
140
150
160
r (mm)
(a)
×10^6
1
0.5
0
-0.5
-1
M_z (A/m)
50
40
30
20
10
0
θ (Mech. deg.)
90
100
110
120
130
140
150
160
r (mm)
(b)

Figure 3

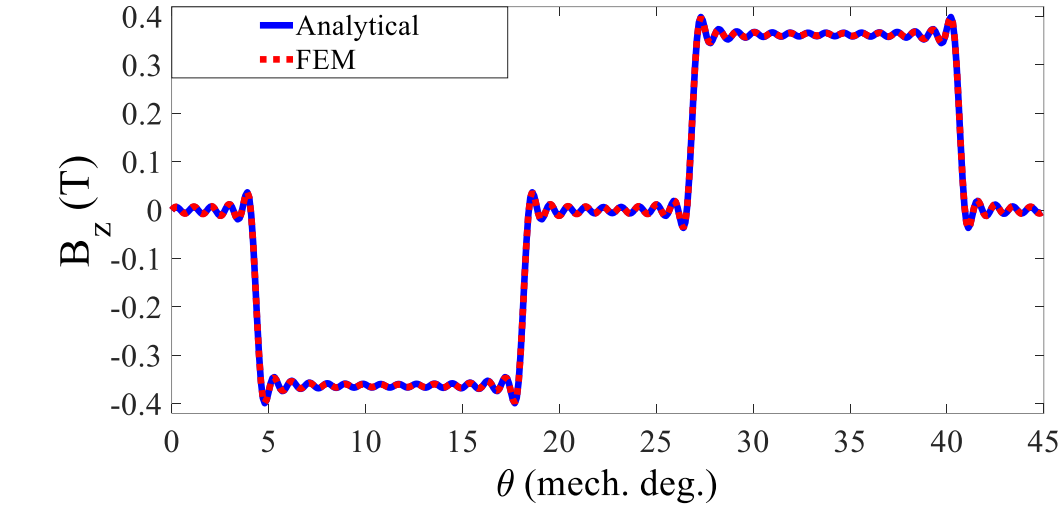
Analytical
FEM
0.4
0.3
0.2
0.1
0
-0.1
-0.2
-0.3
-0.4
B_z (T)
0
5
10
15
20
25
30
35
40
45
θ (mech. deg.)

(a)

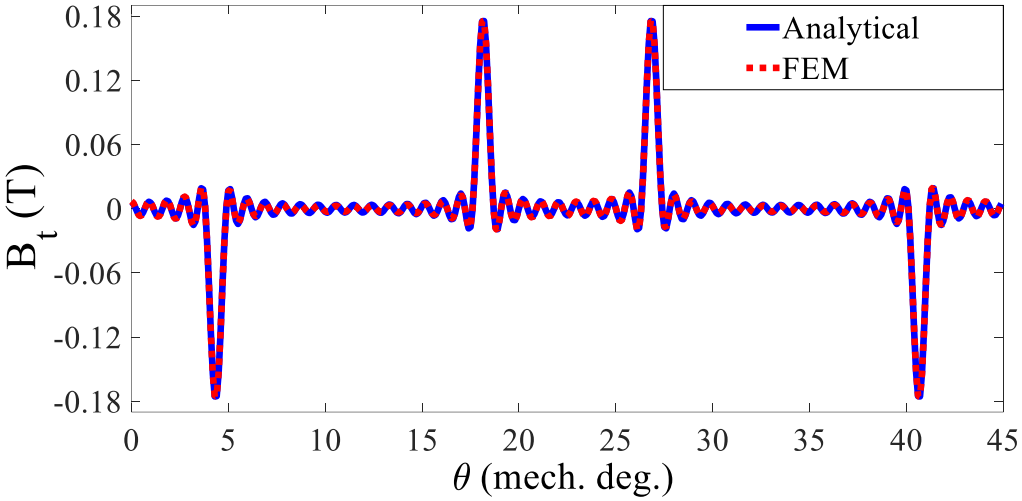
Analytical
FEM
0.18
0.12
0.06
0
-0.06
-0.12
-0.18
B_t (T)
0
5
10
15
20
25
30
35
40
45
θ (mech. deg.)

(b)

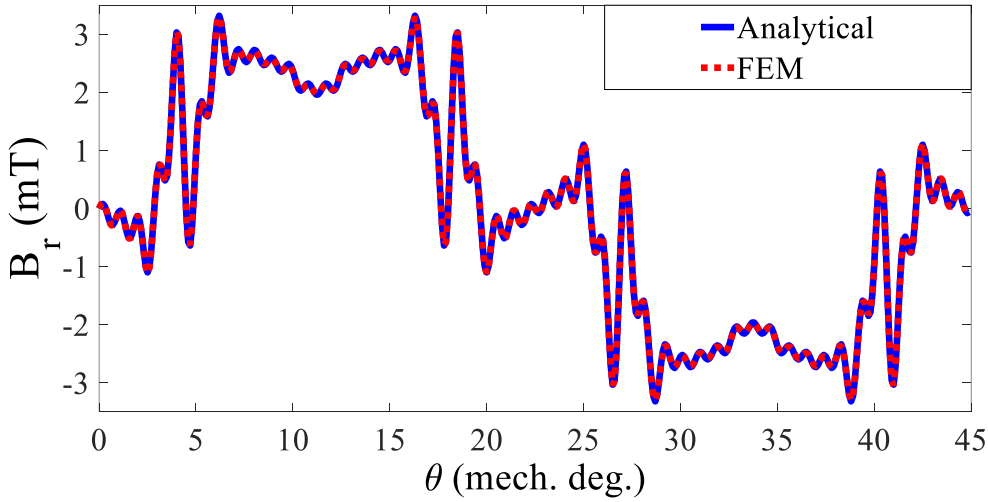
Analytical
FEM
3
2
1
0
-1
-2
-3
B_r (mT)
0
5
10
15
20
25
30
35
40
45
θ (mech. deg.)

(c)

Figure 4

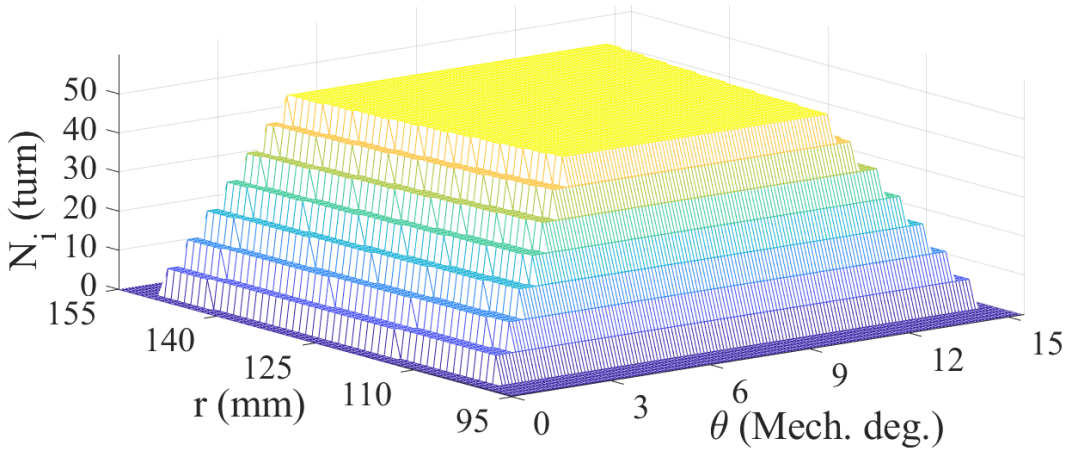
50
40
30
20
10
0
N_i (turn)
155
140
125
110
95
r (mm)
0
3
6
9
12
15
θ (Mech. deg.)

(a)

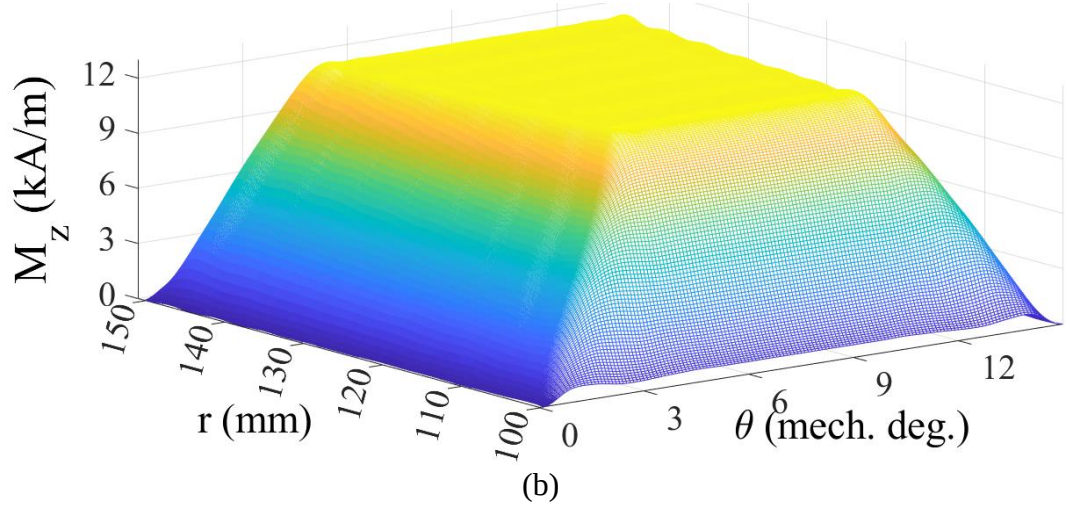
12
9
6
3
0
M_z (kA/m)
150
140
130
120
110
100
r (mm)
0
3
6
9
12
θ (mech. deg.)

(b)

Figure 5

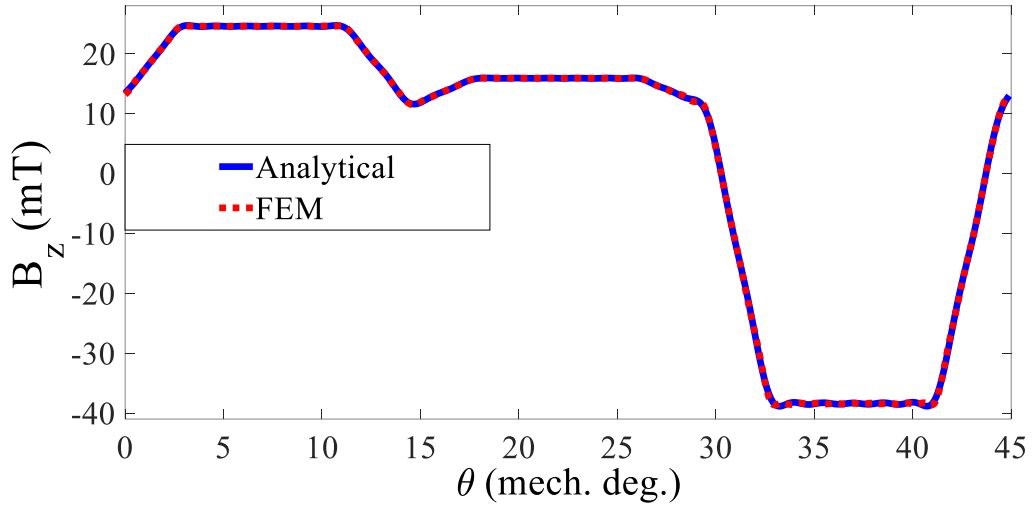
Analytical
FEM
B_z (mT)
θ (mech. deg.)

(a)

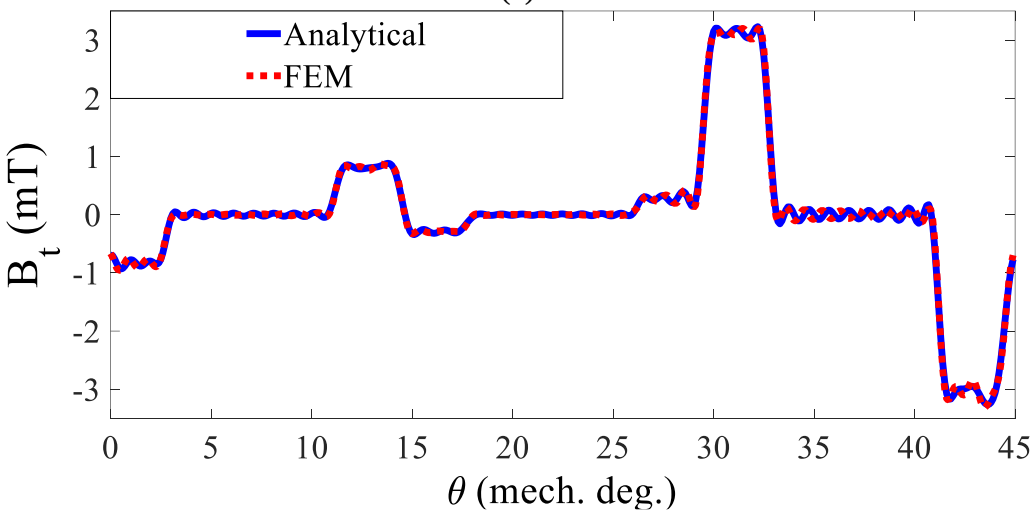
Analytical
FEM
B_t (mT)
θ (mech. deg.)

(b)

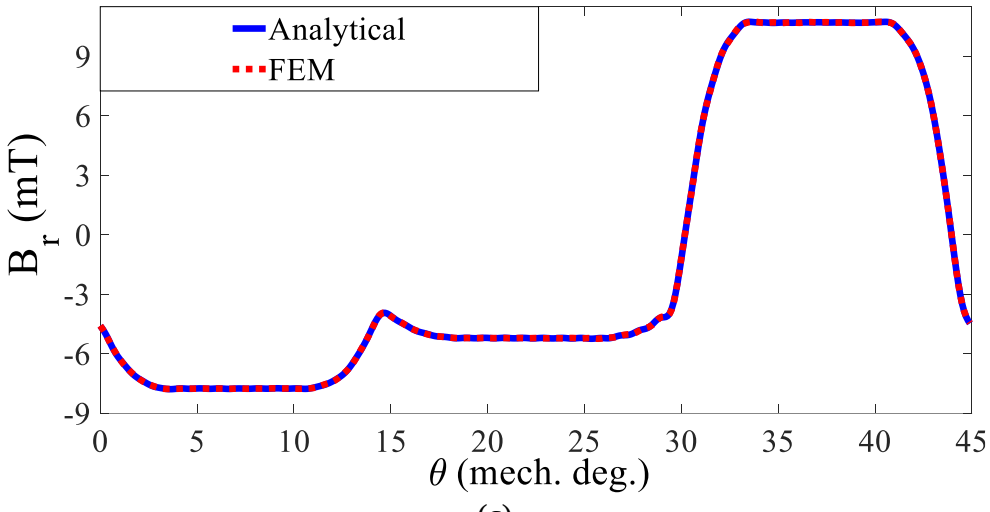
Analytical
FEM
B_r (mT)
θ (mech. deg.)

(c)

Figure 6

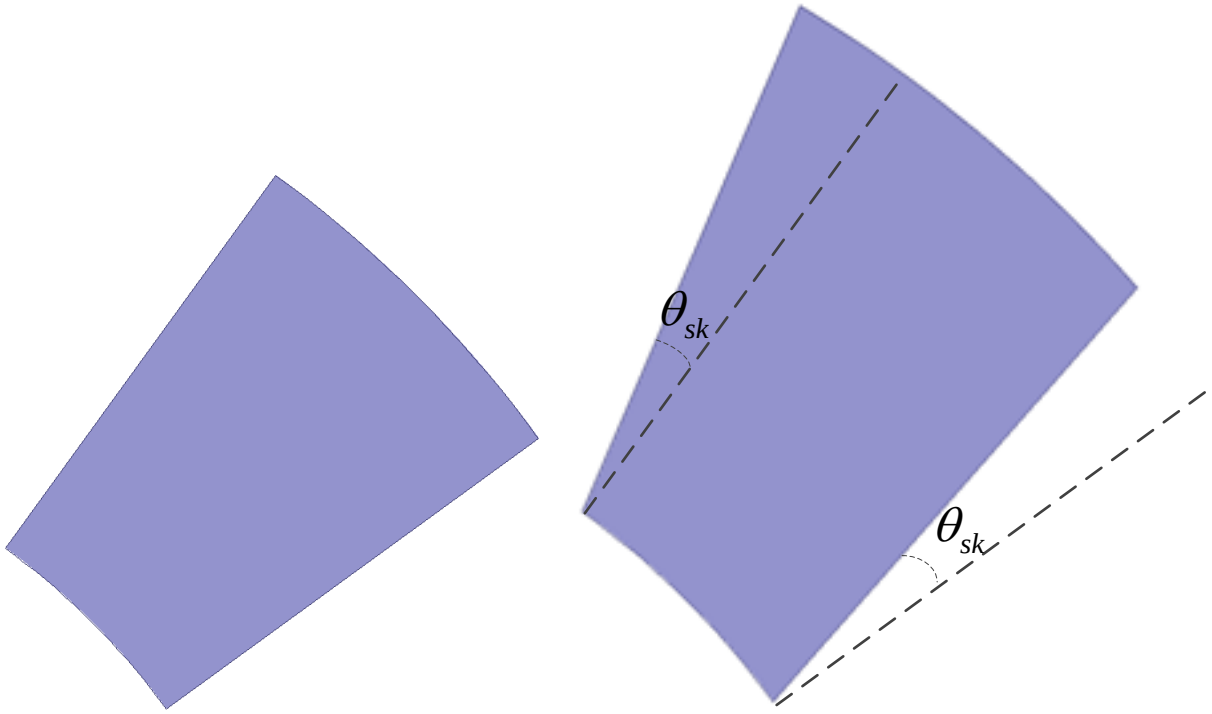

(a) (b)

Figure 7

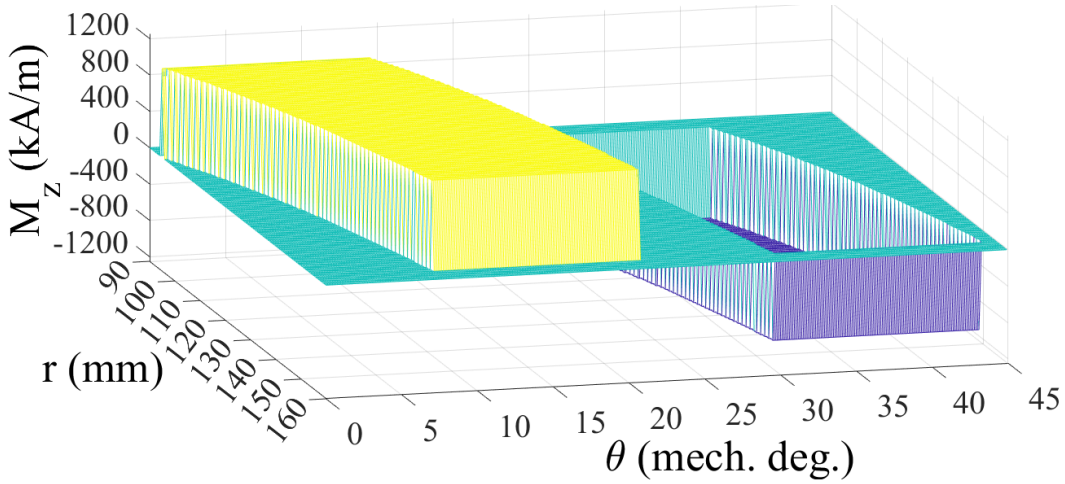
1200
800
400
0
-400
-800
-1200
M_z (kA/m)
90
100
110
120
130
140
150
160
r (mm)
0
5
10
15
20
25
30
35
40
45
θ (mech. deg.)

(a)

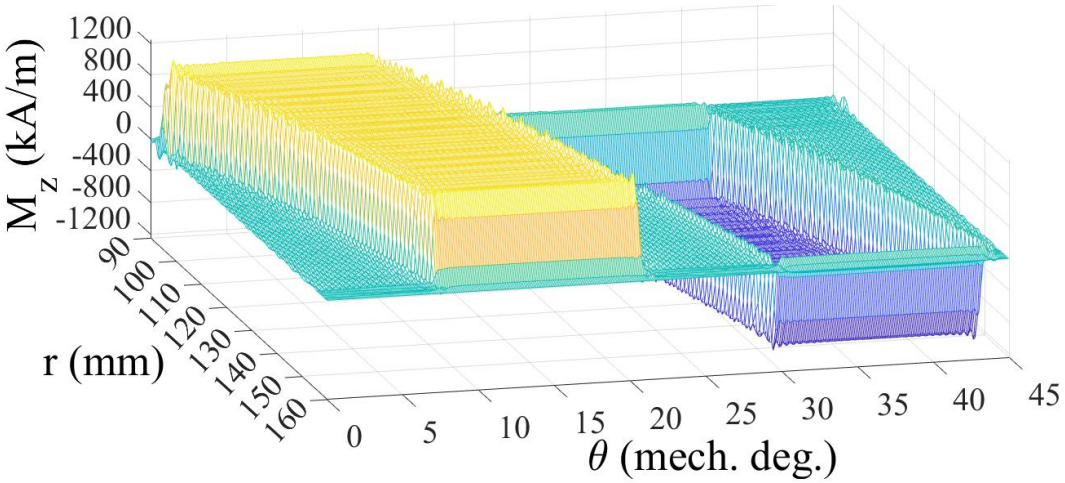
1200
800
400
0
-400
-800
-1200
M_z (kA/m)
90
100
110
120
130
140
150
160
r (mm)
0
5
10
15
20
25
30
35
40
45
θ (mech. deg.)

(b)

Figure 8

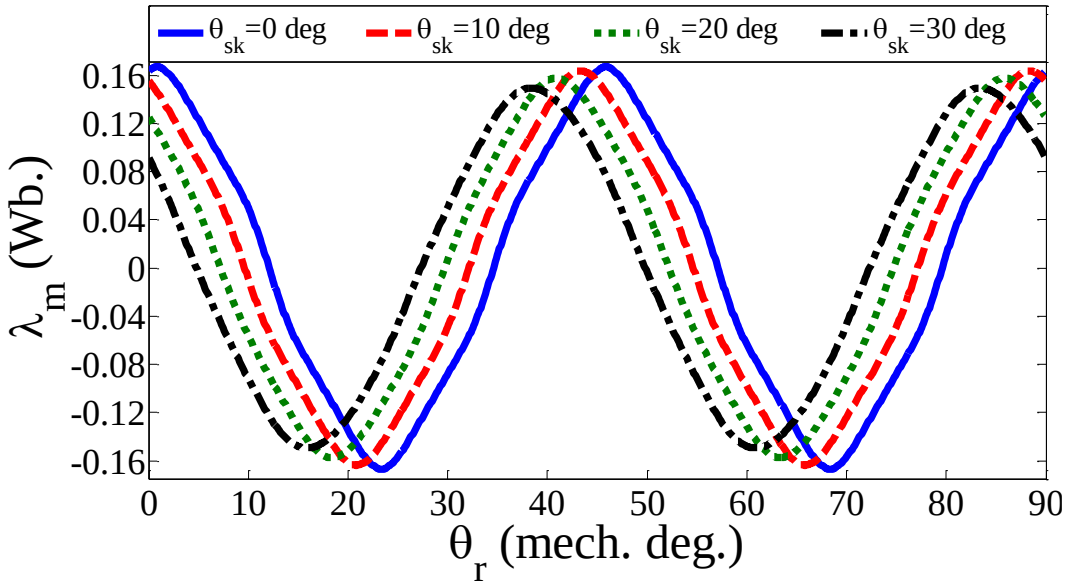
θsk=0 deg
θsk=10 deg
θsk=20 deg
θsk=30 deg
0.16
0.12
0.08
0.04
0
-0.04
-0.08
-0.12
-0.16
λm (Wb.)
0
10
20
30
40
50
60
70
80
90
θr (mech. deg.)

Figure 9

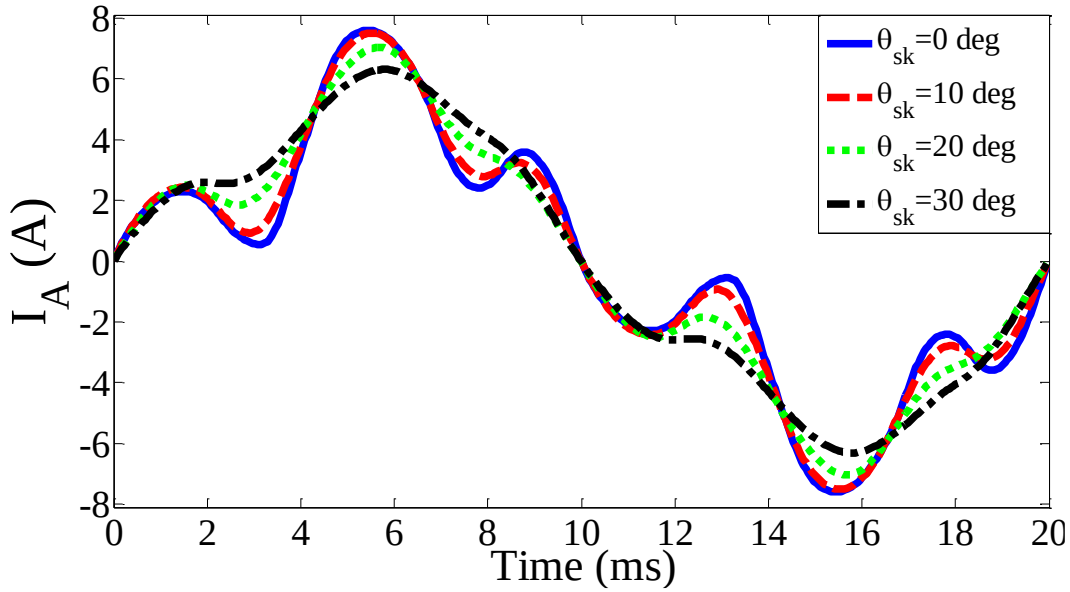
θsk=0 deg
θsk=10 deg
θsk=20 deg
θsk=30 deg
IA (A)
Time (ms)

(a)

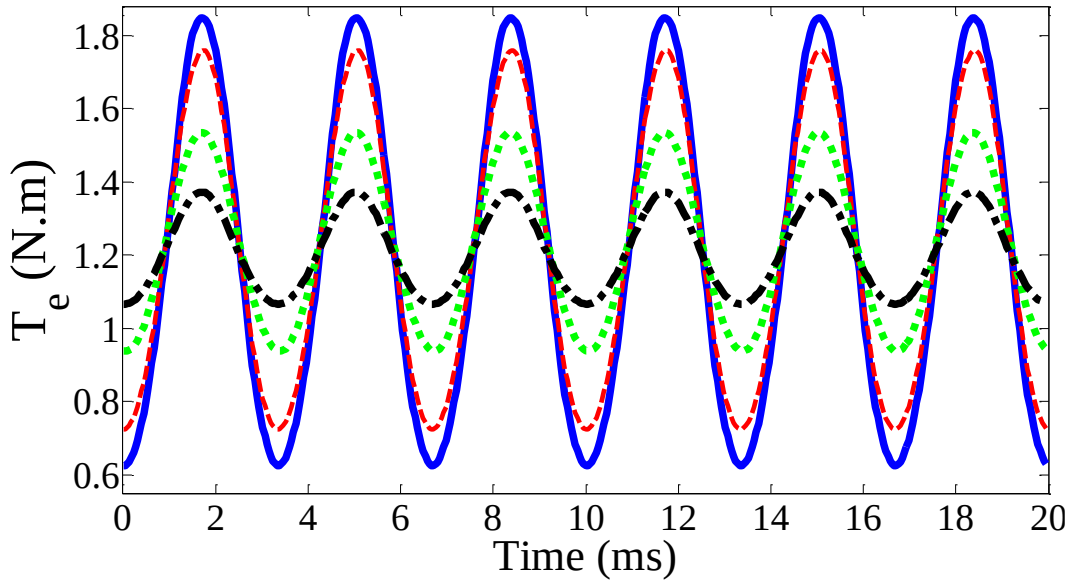
Te (N.m)
Time (ms)

(b)

Figure 10

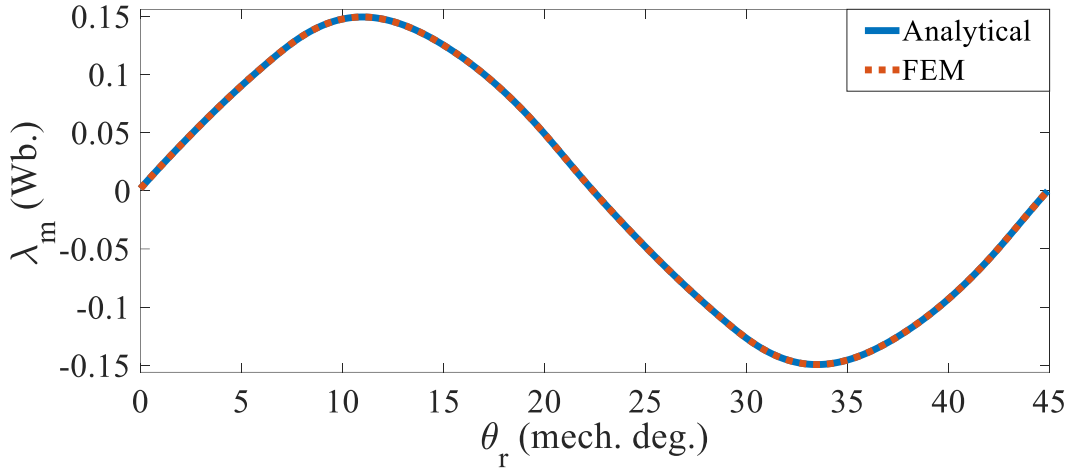

(a)

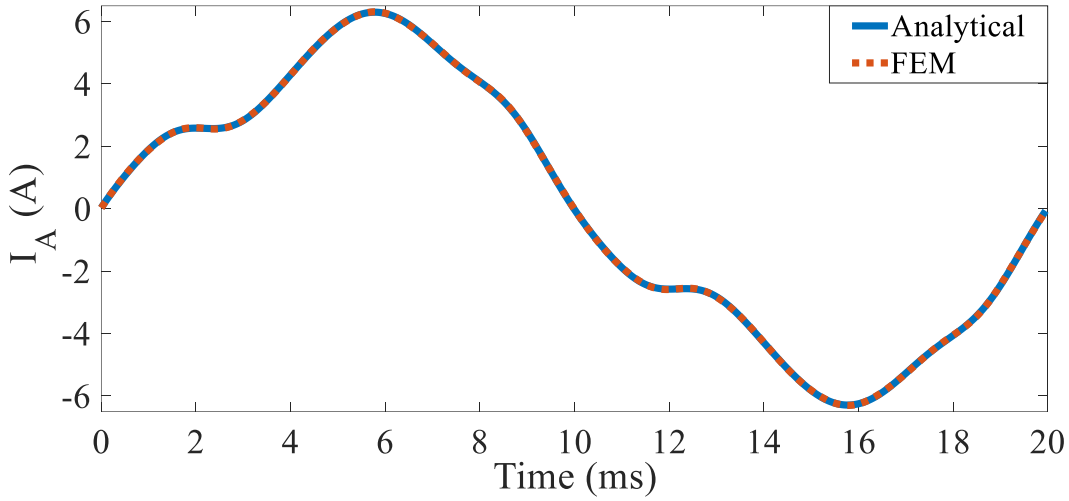

(b)

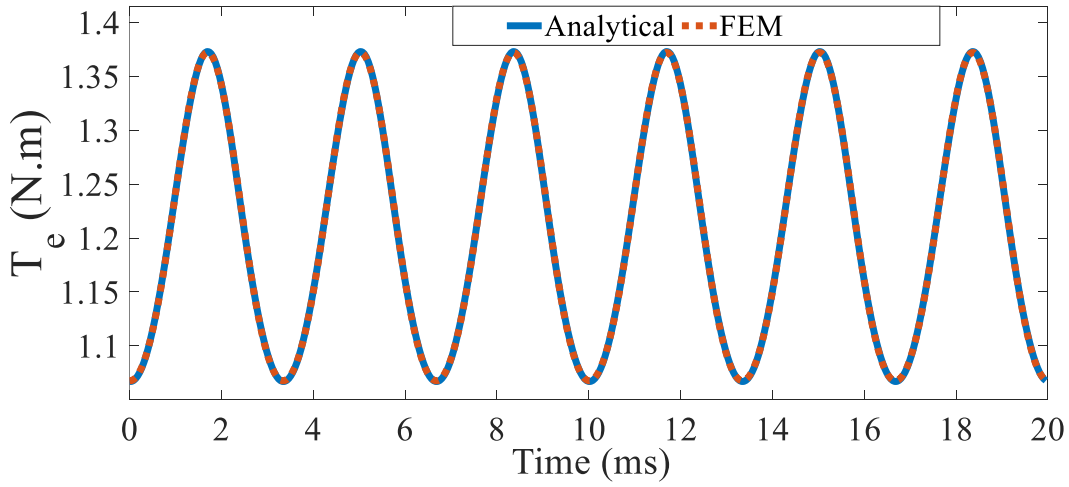

(c)

Figure 11

Table 1

Parameter	Value (Unit)
Outer radius of stator back-iron (r_{so})	150 (mm)
Inner radius of stator back-iron (r_{si})	100 (mm)
Height of stator back-iron	10 (mm)
Number of coils (N_c)	24
Height of coil (h_c)	4 (mm)
Width of coil (w_c)	7 (mm)
Number of coil turns (N_t)	51
Resistance of stator phases (r_s)	1.58 (Ω)
Air-gap length	2 (mm)
Outer radius of PM (r_{mo})	155 (mm)
Inner radius of PM (r_{mi})	95 (mm)
Number of PM poles $(2p)$	16
Height of PM (h_m)	2.5 (mm)
Ratio of pole arc to pole pitch (α_p)	0.8
Outer radius of PM back-iron (r_{ro})	160 (mm)
Inner radius of PM back-iron (r_{ri})	90 (mm)
Height of PM back-iron	10 (mm)
Remanence of PM (B_R)	1.2 (T)
Relative permeability of PM (μ_r)	1.1

Table 2

θ_{sk}	1st harmonic of λ_m(Wb)	THD
0°	0.1555	5.24%
5°	0.1548	5.11%
10°	0.1541	4.59%
15°	0.1528	3.89%
20°	0.1512	3.13%
25°	0.1488	2.48%
30°	0.1462	2.05%

Table 3

θ_{sk}	Power Factor	THD of I_A	Average Torque
0°	0.464 Lag	42.9%	1.2 (N.m)
5°	0.445 Lag	41.8%	1.212 (N.m)
10°	0.424 Lag	37%	1.218 (N.m)
15°	0.392 Lag	31.2%	1.222 (N.m)
20°	0.348 Lag	25.2%	1.226 (N.m)
25°	0.285 Lag	20.3%	1.223 (N.m)
30°	0.21 Lag	16.7%	1.21 (N.m)

Farhad Rezaee-Alam received the B.S. degree from Shahid Chamran University of Ahwaz in 2007, the M.S. and Ph.D. degrees from Khajeh

Nasir University of Technology in 2010 and 2015, respectively, all in electrical engineering. He is currently an associate professor in the department of electrical engineering, Lorestan University, Iran. His research interests include design and modeling of electric machines.
E-mail: rezaee.fa@lu.ac.ir